



BaGeO₃ as sintering additive for BaTiO₃–MgFe₂O₄ composite ceramics

R. Köferstein* and S. G. Ebbinghaus

BaTiO₃–MgFe₂O₄ composites (30 wt% MgFe₂O₄) with a small addition of BaGeO₃ as a sintering additive were synthesized by a one-pot Pechini-like sol–gel process. Nano-crystalline composite powders with a crystallite size of about 10 nm were obtained after reaction at 700 °C for 1 h. Magnetic investigations suggest that the nano-powder is in its superparamagnetic state at room temperature. The addition of BaGeO₃ leads to an improved sintering behaviour. DTA measurements reveal the formation of a liquid phase at 1164(3) °C. Dense ceramic bodies (relative density $\geq 90\%$) were obtained after sintering for 1 h at 1150 °C. SEM investigations prove a 0–3 connectivity and show that the addition of BaGeO₃ promotes the grain growth leading to particles up to 4 μm . In contrast, fine-grained composite ceramics with smaller particles up to 230 nm were obtained after a two-step sintering process. Magnetic measurements indicate a ferrimagnetic behaviour with coercivity values up to 70 Oe depending on the sintering procedure. Furthermore, addition of BaGeO₃ results in an increase of the relative permittivity, whereas the dissipation factor slightly decreases.

Received 25th June 2015
 Accepted 12th August 2015

DOI: 10.1039/c5ra12312g
www.rsc.org/advances

1. Introduction

Multiferroic composite materials are of high interest because of their potential applications in advanced technology *e.g.* as sensors, memories and actuators.^{1–3} Composites consisting of both ferro/ferrimagnetic and ferroelectric phases can exhibit a magneto-electrical (ME) coupling effect.⁴ To produce BaTiO₃–MFe₂O₄ composites (*e.g.* M = Co²⁺, Ni²⁺, Mg²⁺) various synthesis routes have been reported, *e.g.* mixed-oxide-, sol-gel- and hydrothermal processes.^{5–8} Reactions between the BaTiO₃ and MFe₂O₄ phase often lead to the formation of BaFe₁₂O₁₉ and/or hexagonal BaTiO₃.^{9,10} Therefore, the sintering temperature for composite ceramics is limited and depends on the synthesis route and particle size. For some ferrite components, the BaTiO₃–MFe₂O₄ composites show an insufficient sintering behaviour.^{11–13} In particular BaTiO₃–MgFe₂O₄ ceramic bodies exhibit low densities. Up to now this system has rarely been investigated.^{14–17} A magneto-electrical effect in BaTiO₃–MgFe₂O₄ composites was found by Tan *et al.*¹⁴ and Tadi *et al.*¹⁵ As the ME coupling strongly depends on the quality of the oxide interface, dense ceramics with a close contact between the perovskite and spinel phase are advantageous for large ME coefficients. Sintering additives improve the densification, therefore the densities of the ceramic bodies increase and/or the sintering temperature can be reduced.^{18–20} Low sintering temperatures are of special interest as they enable to obtain fine-grained ceramics.

Furthermore, fine-grained ceramics show improved mechanical properties.²¹ The influence of sintering additives on BaTiO₃–MFe₂O₄ ceramics has barely been investigated to date. To our best knowledge, there are only reports on boron- and bismuth-containing fluxes as sintering additives leading to BaTiO₃–MFe₂O₄ glass-ceramic composites.^{22–24} Li *et al.*²⁵ used a Li₂O–Bi₂O₃ flux for fabrication of Pb_{0.88}La_{0.065}Bi_{0.015}Zr_{0.52}Ti_{0.48}O₃–CoFe₂O₄ composites. The formation of a molten phase during sintering usually promotes grain growth and should therefore be avoided if small particle sizes are desired. Previous publications showed that the formation of a molten flux is not necessary to improve the densification of ceramic bodies when sintering additives on the basis of *e.g.* BaGeO₃ and SiO₂ are used.^{19–27}

The aim of this paper is to investigate the influence of BaGeO₃ as sintering additive on BaTiO₃–MgFe₂O₄ composite ceramics with a 0–3 connectivity. The samples were synthesized using a one-pot sol–gel method leading to nano-sized powders. Phase formation during the sintering process was monitored by XRD and thermal analysis. The sintering behaviour and micro-structure of resulting compacts were determined by dilatometry and SEM. Magnetic measurements were carried out both on composite powders and ceramic bodies. Furthermore, the influence of BaGeO₃ on the dielectric behaviour was studied.

2. Experimental

2.1. Material preparation

Composites with a weight fraction of $0.7 \times (\text{BaTi}_{0.95}\text{Ge}_{0.05}\text{O}_3) - 0.3 \times (\text{MgFe}_2\text{O}_4)$ ($= 33\text{ mol\% or } 36\text{ vol\% MgFe}_2\text{O}_4$) were prepared using a modified Pechini-like sol–gel process as described



elsewhere.¹⁷ This composition is abbreviated as $\text{BT}_{0.95}\text{G}_{0.05}\text{-MF-0.3}$ in the following. Additionally composites with the composition $0.7 \times (\text{BaTi}_{0.9}\text{Ge}_{0.1}\text{O}_3) - 0.3 \times (\text{MgFe}_2\text{O}_4)$ (donated as $\text{BT}_{0.9}\text{G}_{0.1}\text{-MF-0.3}$) and a Ti-excess composite $0.7 \times (\text{BaTi}_{1.0}\text{Ge}_{0.05}\text{O}_3) - 0.3 \times (\text{MgFe}_2\text{O}_4)$ (donated as $\text{BT}_{1.0}\text{G}_{0.05}\text{-MF-0.3}$) were synthesized.

$\text{BT}_{0.95}\text{G}_{0.05}\text{-MF-0.3}$ composites were obtained by dissolving 0.01250 mol freshly distilled $\text{Ti}(\text{OC}_3\text{H}_7)_4$ (Aldrich), 0.00066 mol $\text{Ge}(\text{OC}_2\text{H}_5)_4$ (Alfa Aesar), 0.01316 mol BaCO_3 (Merck 1713, extra pure) and 0.127 mol anhydrous citric acid in 30 g 1,2-ethanediol at 70 °C leading to a clear solution. Stoichiometric proportions of 0.00661 mol $\text{Mg}(\text{NO}_3)_3 \cdot 6\text{H}_2\text{O}$ (Alfa Aesar) and 0.01322 mol $\text{Fe}(\text{NO}_3)_3 \cdot 9\text{H}_2\text{O}$ (Merck) were dissolved in 25 g 1,2-ethanediol and added to the above solution. The resulting mixture was continuously stirred at about 190–200 °C until it turned to a black-brown viscous gel. This gel was calcined in static air at 700 °C for 1 h (heating/cooling rate 5 K min⁻¹).

The other compositions were prepared by the same procedure using corresponding stoichiometric quantities.

To obtain ceramic bodies, the calcined powders were uniaxially pressed at about 85 MPa into pellets (green density 2.0 g cm⁻³) without using any pressing aid or binder. These pellets were placed on a ZrO_2 fibre mat. Two different sintering procedures were used; conventional sintering (heating up with 10 K min⁻¹, soaking at this temperature, cooling down with 10 K min⁻¹) and two-step sintering (heating up with 20 K min⁻¹ to 1150 °C (T_1), then fast cooled with 30 K min⁻¹ to a lower temperature T_2 and held at T_2 for 20 h).

2.2. Characterization

X-ray powder diffraction patterns were collected at room temperature on a *Bruker D8-Advance* diffractometer, equipped with a one-dimensional silicon strip detector (LynxEyeTM) and operating with Cu-K_α radiation. Crystallite sizes were determined from the XRD line broadening using the Scherrer equation and the integral peak breadth (software suite WinXPOW²⁸). Dilatometric investigations were performed in flowing synthetic air (50 ml min⁻¹) in a *Setaram TMA 92-16.18* dilatometer. Differential thermoanalytic (DTA) measurements in flowing synthetic air (20 ml min⁻¹) were done using a *Netzsch STA 449* system. Scanning electron microscope images were recorded with a *Philips XL30 ESEM* in the backscattered electron mode (BSE). For magnetic measurements a *Quantum Design PPMS 9* was used. Hysteresis loops were obtained with magnetic field cycling between -90 and +90 kOe. In addition, the temperature dependent magnetic moments were measured in the temperature range of 5–300 K under field-cooled (FC) and zero-field-cooled (ZFC) conditions. An Impedance Analyzer 4192A (Hewlett Packard) was used for permittivity measurements up to 13 MHz. A eutectic Ga-In alloy was applied as electrical contact on both sides of the ceramic bodies.

3. Results and discussion

3.1. Powder characterization

In a previous paper¹⁷ we reported on the preparation of $(1 - x)\text{BaTiO}_3 - x\text{MgFe}_2\text{O}_4$ composites (x = weight fraction) with

0–3 connectivity *via* a Pechini-like process. The $\text{BaTiO}_3\text{-MgFe}_2\text{O}_4$ composite powders were found to have an insufficient sintering behaviour resulting in ceramic bodies with moderate densities of about 70% at 1200 °C. The maximum sintering temperature for $\text{BaTiO}_3\text{-MgFe}_2\text{O}_4$ systems is limited because of the formation of hexagonal BaTiO_3 and/or $\text{BaFe}_{12}\text{O}_{19}$.^{9,17,29} As stated in ref. 30 and 31 the densification of BaTiO_3 can be improved using BaGeO_3 as sintering additive. Guha and Kolar³² found that a maximum of 1.8 mol% Ge^{4+} (related to the occupation of the Ti^{4+} site) can be incorporated into the BaTiO_3 lattice. For our investigations a much higher content of ≥ 5 mol% BaGeO_3 was used, resulting predominantly in a mixture of (Ge-doped) BaTiO_3 and BaGeO_3 . For simplicity this composition is described by the formula $\text{BaTi}_{0.95}\text{Ge}_{0.05}\text{O}_3$ in the following.

The first step of the Pechini-like sol-gel process leads to highly-viscous homogeneous gels in which the metal ions are mixed on a molecular level. To obtain composite powders, these dark-brown gels were calcined at 700 °C for 1 h. The XRD pattern of the resulting powder shows mainly reflections of BaTiO_3 , MgFe_2O_4 , and only small amounts of BaCO_3 (ref. 33) (Fig. 1). After this first heat treatment no peaks related to Ge-containing phases could be detected. As an example, the powder $0.7 \times (\text{BaTi}_{0.95}\text{Ge}_{0.05}\text{O}_3) - 0.3 \times (\text{MgFe}_2\text{O}_4)$ (donated as $\text{BT}_{0.95}\text{G}_{0.05}\text{-MF-0.3}$) was examined by the BET method and was found to possess a specific surface area of 34.5 m² g⁻¹, corresponding to an equivalent particle size of 32 nm. The volume-weighted average crystallite sizes for both the MgFe_2O_4 and the BaTiO_3 phase were calculated as 10 nm from XRD line broadening. The calculated crystallite size is roughly by the factor three smaller than the size of the primary particles obtained from the BET data. This is most likely because the decomposition of the gel leads to closely joined crystallites and in turn surface areas unavailable for nitrogen adsorption.³⁴ An alternative explanation is that each primary particle may consist of several crystallite domains.

Temperature-dependent magnetic investigations ($H = 500$ Oe) show a superparamagnetic behaviour for the $\text{BT}_{0.95}\text{G}_{0.05}\text{-MF-0.3}$ powder (Fig. 2A). The field-cooled (FC) curve

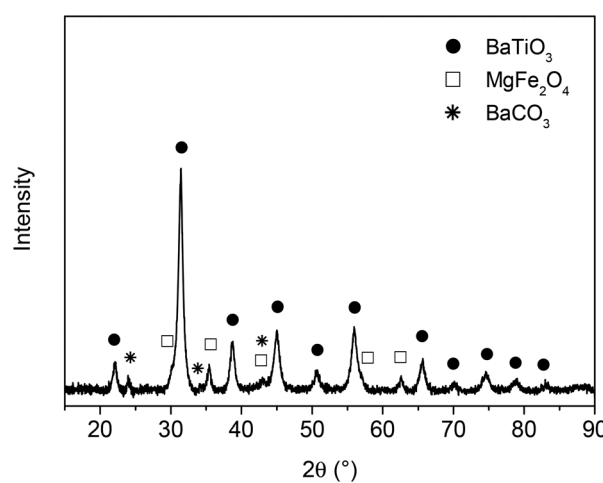


Fig. 1 Room temperature XRD pattern of the powder $\text{BT}_{0.95}\text{G}_{0.05}\text{-MF-0.3}$ calcined at 700 °C for 1 h.



increases continuously with decreasing temperature, while the zero-field-curve (ZFC) curve has a maximum at 20 K, the so called blocking temperature. The superparamagnetic behaviour is confirmed by field-dependent magnetic measurements. At 300 K the coercivity value is close to zero, whereas below the blocking temperature the hysteresis loop at 5 K shows a coercivity value of 146 Oe (Fig. 2B).

3.2. Composite ceramics

DTA investigations (shown in Fig. 3) of $\text{BT}_{0.95}\text{G}_{0.05}\text{-MF-0.3}$ and $\text{BT}_{0.9}\text{G}_{0.1}\text{-MF-0.3}$ samples show the formation of a liquid phase (Graph 3a,b). The DTA signal increases with rising BaGeO_3 content. The onset temperature of the melting peak was determined as $1164(3)$ °C. In contrast, the $\text{BT}\text{-MF-0.3}$ composite without BaGeO_3 does not reveal any DTA signal up to 1200 °C (Graph 3c).

Fig. 4 shows the non-isothermal dilatometric measurement up to 1200 °C in flowing air of compacts from powder $\text{BT}_{0.95}\text{G}_{0.05}\text{-MF-0.3}$ and $\text{BT}\text{-MF-0.3}$ calcined at 700 °C for 1 h, respectively. The shrinkage process of $\text{BT}_{0.95}\text{G}_{0.05}\text{-MF-0.3}$ (Graph 4a) starts at about 800 °C and the shrinkage rate achieves a maximum at 1102 °C with a value of -1.68 % min^{-1} . Interestingly, this shrinkage maximum occurs below the liquid phase formation at 1164 °C. The shrinkage rate indicates that

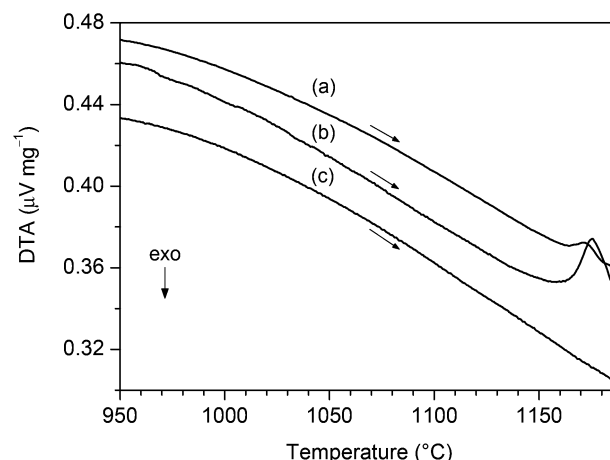


Fig. 3 DTA measurements in flowing air (10 K min^{-1}) of (a) $\text{BT}_{0.95}\text{G}_{0.05}\text{-MF-0.3}$, (b) $\text{BT}_{0.9}\text{G}_{0.1}\text{-MF-0.3}$, and (c) $\text{BT}\text{-MF-0.3}$.

the densification is dominated by sliding processes (viscous flow). Diffusion as the dominant process causes only shrinkage rates of about 10^{-4} to $10^{-1}\text{ % min}^{-1}$.³⁵⁻³⁸ Investigations on the $\text{BaTiO}_3\text{-BaGeO}_3$ system confirm that the addition of BaGeO_3 promotes sliding processes.³⁹ The shrinkage has not yet been finished at the highest investigated temperature of 1200 °C. For comparison graph 4b shows the shrinkage behaviour of $\text{BT}\text{-MF-0.3}$ compacts without the addition of BaGeO_3 . A maximum of the shrinkage rate can be observed at 1185 °C (-0.80 % min^{-1}). Thus the addition of BaGeO_3 leads to improved shrinkage behaviour at relatively low temperatures without involvement of a molten phase.

Fig. 5 shows the final bulk densities of ceramic bodies after isothermal conventional sintering at various temperatures in static air (heating up with 10 K min^{-1} , soaking at this temperature for 1 h, cooling down with 10 K min^{-1}). The absolute bulk densities of the sintered bodies were determined from their

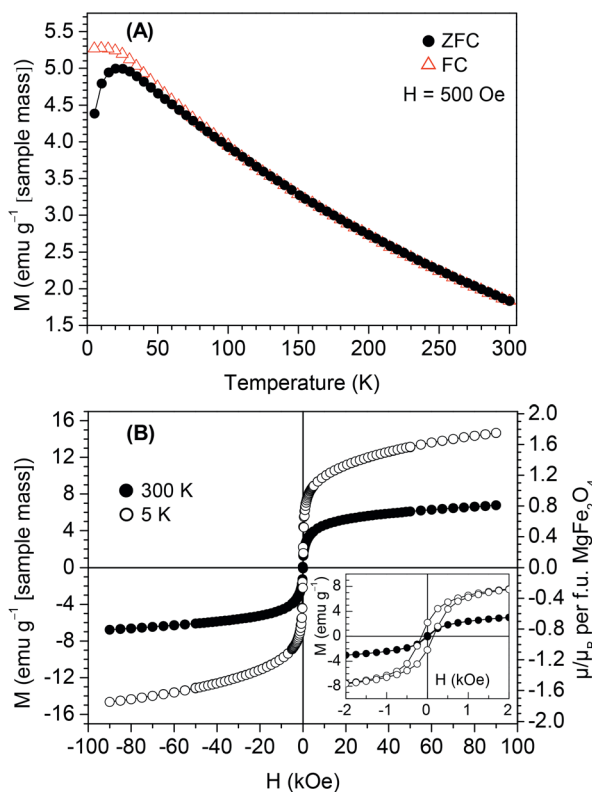


Fig. 2 (A) Temperature dependence (5–300 K) of the magnetization under zero-field cooled (ZFC) and field-cooled (FC) conditions for powder $\text{BT}_{0.95}\text{G}_{0.05}\text{-MF-0.3}$ calcined at 700 °C. (B) Magnetization (M) versus applied magnetic field (H) at 300 and 5 K for $\text{BT}_{0.95}\text{G}_{0.05}\text{-MF-0.3}$ powder. The inset shows M versus H in a small field range.

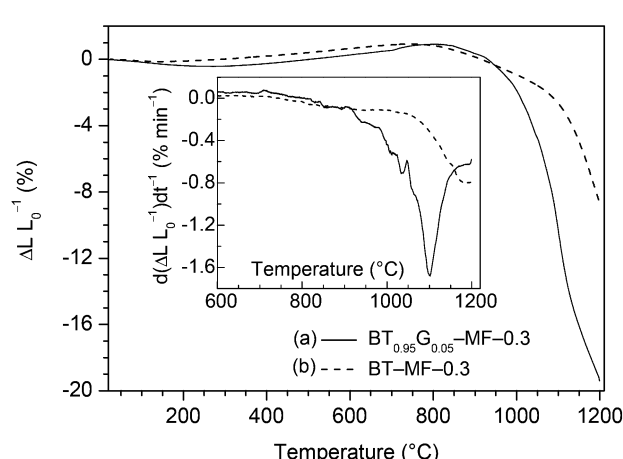


Fig. 4 Non-isothermal dilatometric measurements in flowing air for compacts of $\text{BT}_{0.95}\text{G}_{0.05}\text{-MF-0.3}$ and $\text{BT}\text{-MF-0.3}$ (calcined at 700 °C) with a heating rate of 10 K min^{-1} . The inset shows the relative shrinkage rates ($d\Delta L_0^{-1}/dt^{-1}$).

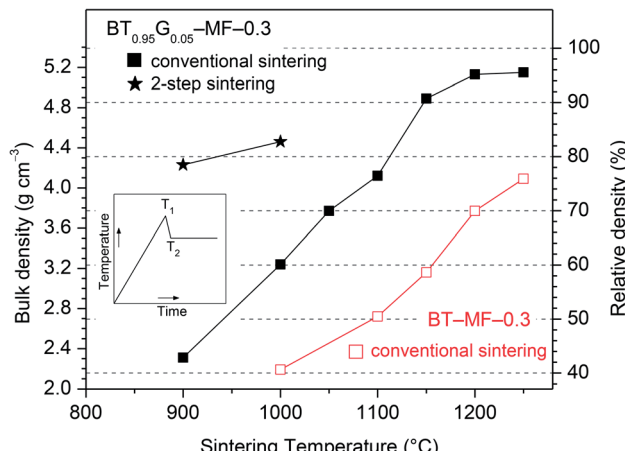


Fig. 5 Bulk densities of conventional (■ □, soaking time 1 h) and two-step sintered (★, soaking time 20 h) ceramic bodies from $\text{BT}_{0.95}\text{G}_{0.05}\text{-MF-0.3}$ and $\text{BT}\text{-MF-0.3}$ powders calcined at 700 °C. The inset schematically shows the two-step sintering process.

weight and geometric dimensions. The relative bulk densities of all ceramic bodies were calculated with respect to the theoretical density of 5.39 g cm^{-3} for $\text{BT}\text{-MF-0.3}$.^{17,31} It turned out that $\text{BT}_{0.95}\text{G}_{0.05}\text{-MF-0.3}$ ceramic bodies with relative densities of 70% can be obtained even at 1050 °C. By raising the sintering temperature to 1150 °C dense ceramics with 91% relative density can be achieved. After sintering at 1200 °C the relative density further increases to 95%. According to the DTA results sintering above 1150 °C is characterized by liquid-phase sintering processes. As seen in Fig. 5 the formation of a liquid-phase is not necessary to obtain dense ceramic bodies.

Longer sintering times have little influence on the density. For example, a soaking time of 10 h at 1100 °C results only in minor increase of the relative density from 76 to 79% for $\text{BT}_{0.95}\text{G}_{0.05}\text{-MF-0.3}$ composites. Furthermore, an increase of the BaGeO_3 content to 10 mol% ($\text{BT}_{0.9}\text{G}_{0.1}\text{-MF-0.3}$) does not lead to rising densities. After sintering at 1100 °C for 1 h ceramic bodies of $\text{BT}_{0.9}\text{G}_{0.1}\text{-MF-0.3}$ with a relative density of 69% (3.71 g cm^{-3}) were obtained. On the other hand, BaGeO_3 -free $\text{BT}\text{-MF-0.3}$ ceramics reach relative densities of only 50 and 70% after sintering at 1100 and 1200 °C for 1 h, respectively.

The SEM images of $\text{BT}_{0.95}\text{G}_{0.05}\text{-MF-0.3}$ ceramic bodies depicted in Fig. 6 show a 0–3 connectivity between the spinel and the perovskite phase. In the applied BSE mode the light grains correspond to BaTiO_3 while the dark grains are MgFe_2O_4 . Sintering at 1000 °C results in grain sizes between about 90 and 200 nm, which only slightly increase to 140–350 nm after sintering at 1100 °C (Fig. 6a). Up to this temperature there is no significant size difference between the BaTiO_3 and MgFe_2O_4 grains. In contrast, sintering at 1150 °C for 1 h leads to a considerable grain growth with BaTiO_3 grains in the range between 0.25–0.9 μm and MgFe_2O_4 grains between 0.25 and 3 μm as seen in Fig. 6b. Abnormal grain growth occurs during sintering at 1200 °C resulting in BaTiO_3 grain sizes between 0.5 and 1.5 μm while the size of the ferrite grains ranges between 0.5 and 4 μm. The appearance of white rods with

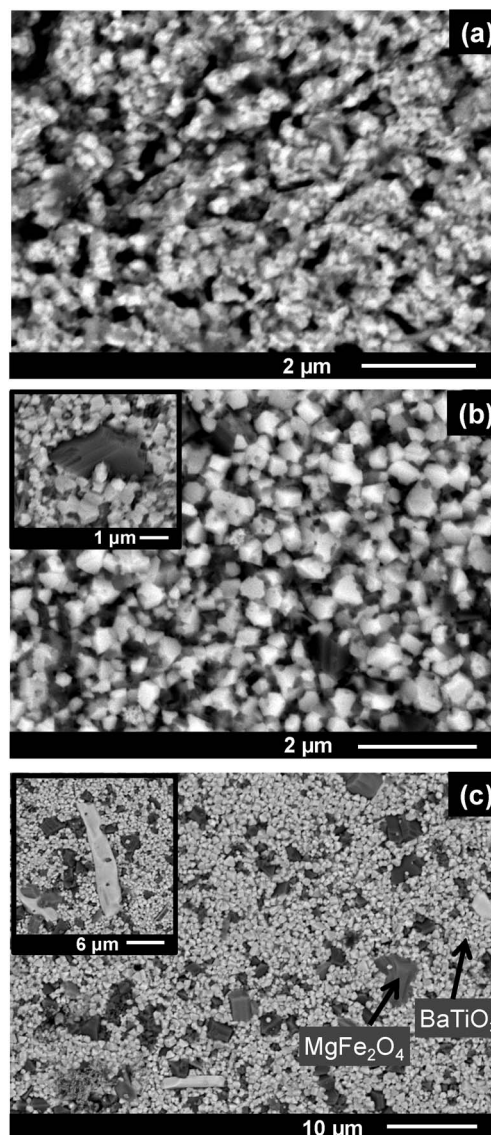


Fig. 6 SEM-BSE images of ceramic bodies sintered at (a) 1100 °C, 1 h, (b) 1150 °C, 1 h, and (c) 1200 °C, 1 h.

dimensions up to $23 \times 4 \mu\text{m}$ after sintering at 1200 °C indicates the formation of hexagonal BaTiO_3 (ref. 40) (Fig. 6c) in accordance with the XRD results discussed below.

Using a two-step sintering procedure the densification at lower temperatures can be improved.^{30,41} In this approach, the compacts were first heated rapidly (20 K min^{-1}) to 1150 °C (T_1), then fast cooled (30 K min^{-1}) to a lower temperature T_2 and held at T_2 for 20 h (see inset in Fig. 5). Two-step sintering with $T_2 = 900$ °C leads to a relative bulk density of 78% (4.23 g cm^{-3}), whereas upon rising T_2 to 1000 °C the ceramic bodies achieve a relative density of 83% (4.46 g cm^{-3}). In both cases the ceramic bodies consists of grain between about 90 and 230 nm. For comparison, conventional sintering at 1000 °C for 20 h leads only to a relative density of 68%.

XRD powder patterns of selected $\text{BT}_{0.95}\text{G}_{0.05}\text{-MF-0.3}$ ceramics are shown in Fig. 7. The pattern of ceramics sintered



up to 1100 °C shows only reflections of BaTiO₃ and MgFe₂O₄. At 2θ ≈ 45° no clear splitting of the BaTiO₃ (002)/(200) peak could be detected indicating a reduced tetragonality, *i.e.* a considerable lower *c/a* ratio compared to coarse-grained ceramics with more than 1 μm particles. After sintering at 1150 °C very small traces of BaFe₁₂O₁₉ appear,³³ whereas after 1200 °C about 19 mol% of BaTiO₃ has been converted to the hexagonal modification. Sintering at 1250 °C leads to an increase of hexagonal BaTiO₃ to 54 mol%. The formation of the hexagonal BaTiO₃ modification at such comparably low temperatures is noteworthy since in pure BaTiO₃ samples the transition to the hexagonal structure occurs above 1460 °C.⁴² The formation of hexagonal BaTiO₃ at lower temperatures in the composites is probably caused by the incorporation of small amounts of iron- and magnesium-ions into the BaTiO₃ lattice.^{43–47} Peaks corresponding to BaGeO₃ were not found, most likely because of its small content. In contrast, BT_{0.9}G_{0.1}–MF–0.3 ceramic bodies with their larger BaGeO₃ content clearly show the formation of monoclinic α-BaGeO₃ (ref. 33) (Fig. 8A, Graph a).

To suppress the formation of hexagonal BaTiO₃ an excess of 5 mol% Ti, with respect to the Ba-content, was used in the BT_{1.0}G_{0.05}–MF–0.3 composite ceramics. As seen in Fig. 8A (Graph b) after sintering at 1200 °C no reflections of hexagonal BaTiO₃ are detectable. Whereas, after sintering at 1250 °C of BT_{1.0}G_{0.05}–MF–0.3 the fraction of hexagonal BaTiO₃ is not completely suppressed but reduced from 54 mol% to 31 mol% (Fig. 8A, Graph c). Therefore, at higher sintering temperatures an excess of more than 5 mol% Ti is needed to completely avoid the formation of hexagonal BaTiO₃. On the other hand, the titanium excess leads to an increase of BaFe₁₂O₁₉ as seen in Fig. 8B. This finding is in accordance with investigations by van den Boomgaard and Born¹⁰ on BaTiO₃–Ni(Co,Mn)Fe₂O₄ composites that showed a continuous increase of BaFe₁₂O₁₉ with rising titanium excess, most likely caused by the partial replacement of Fe³⁺ ions in BaFe₁₂O₁₉ by Ti⁴⁺.^{48,49}

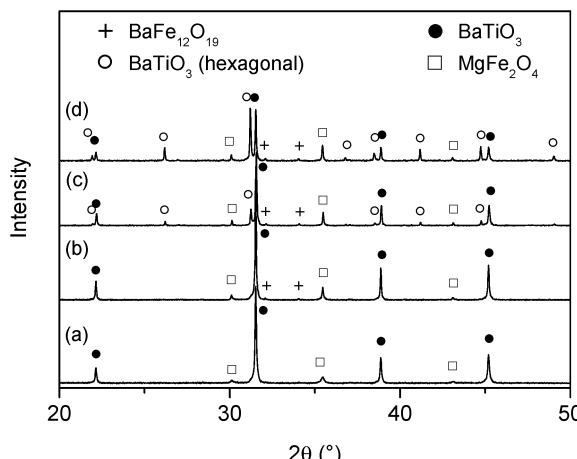


Fig. 7 Room temperature XRD patterns of BT_{0.95}G_{0.05}–MF–0.3 ceramic bodies after sintering for 1 h (rate: 10 K min^{−1}). (a) 1100 °C (b) 1150 °C, (c) 1200 °C, (d) 1250 °C. For clarity only a section of the measured range is shown.

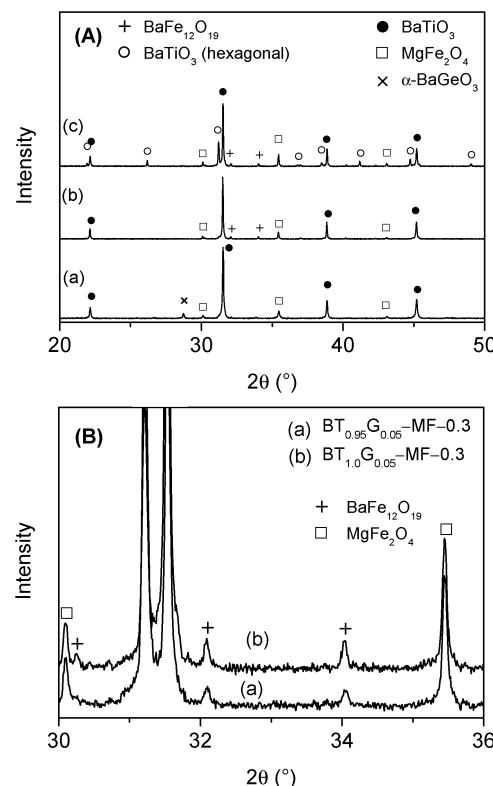


Fig. 8 (A) Room temperature XRD patterns of ceramics after sintering of 1 h of (a) BT_{0.9}G_{0.1}–MF–0.3 sintered at 1100 °C, (b) BT_{1.0}G_{0.05}–MF–0.3 sintered at 1200 °C, and (c) BT_{1.0}G_{0.05}–MF–0.3 sintered at 1250 °C. For clarity only a section of the measured range is shown. (B) Detail of the XRD patterns in the range of 2θ = 30–36° of BT_{0.95}G_{0.05}–MF–0.3 and BT_{1.0}G_{0.05}–MF–0.3 sintered at 1250 °C.

3.3. Magnetic and dielectric measurements of ceramic bodies

Fig. 9A shows the *M*–*H* loops at 300 K of BT_{0.95}G_{0.05}–MF–0.3 ceramic bodies conventionally sintered between 1000 and 1200 °C for 1 h. Small coercivity values (*H*_c) up to 64 Oe and saturation magnetizations (*M*_s) of 7.9–9.1 emu g^{−1} were observed. *M*_s values were calculated by a linear extrapolation of the magnetization at highest field to *H* = 0, assuming the increase in magnetization at high-field is dominated by a paramagnetic contribution (see below). The values of *H*_c and *M*_s depend on the sintering temperature as seen in Fig. 9B. The coercivity values show a maximum at 1100 °C, whereas the *M*_s only slightly decreases for samples sintered between 1000 °C and 1100 °C. Sintering at higher temperatures leads to a stronger decrease of *M*_s. The reduction of *M*_s is probably due to the reaction between BaTiO₃ and MgFe₂O₄. On the other hand cation redistribution between Mg²⁺ and Fe³⁺ and thus a change of the inversion parameter is also possible because a similar behaviour was observed in pure MgFe₂O₄ samples, too.⁵⁰

Two-step sintering with *T*₂ = 1000 °C and 900 °C leads to similar hysteresis loops at 300 K, which are characterized by *M*_s = 9.1 emu g^{−1} and *H*_c = 68 and 70 Oe, respectively (not shown).

Temperature-dependent magnetic measurements with an applied field of *H* = 60 kOe of a BT_{0.95}G_{0.05}–MF–0.3 ceramic



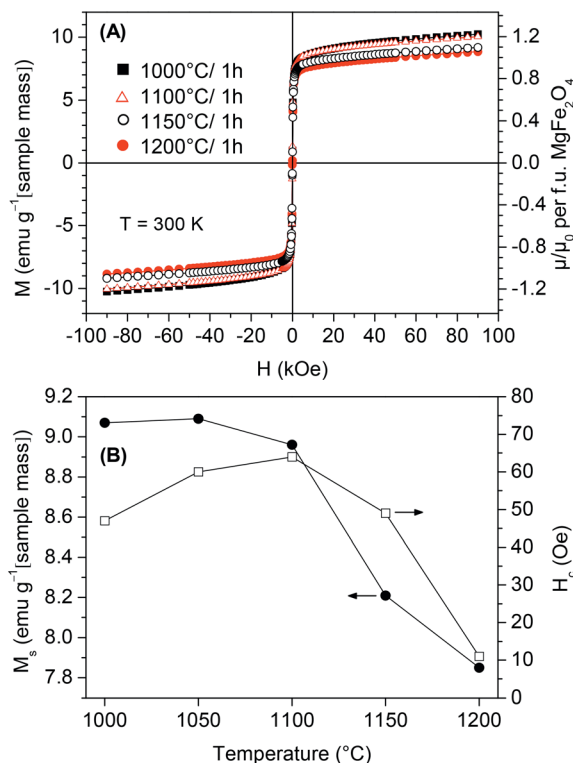


Fig. 9 (A) Magnetization (M) versus applied magnetic field (H) at 300 K for BT_{0.95}G_{0.05}-MF-0.3 ceramic bodies conventionally sintered at the indicated temperatures for 1 h. (B) Dependence of the saturation magnetization (M_s) and coercivity (H_c) on the sintering temperature (soaking time 1 h).

sintered at 1000 °C show identical values under FC and ZFC conditions, therefore in Fig. 10 only the FC curve is presented. A slight increase at lowest temperatures was found in contrast to a pure MgFe₂O₄ ceramic sample indicating a minor paramagnetic contribution in the composites. This small paramagnetic moment is probably caused by diffusion of Fe-ions at the grain boundaries from the MgFe₂O₄ to the BaTiO₃ phase.^{51–53}

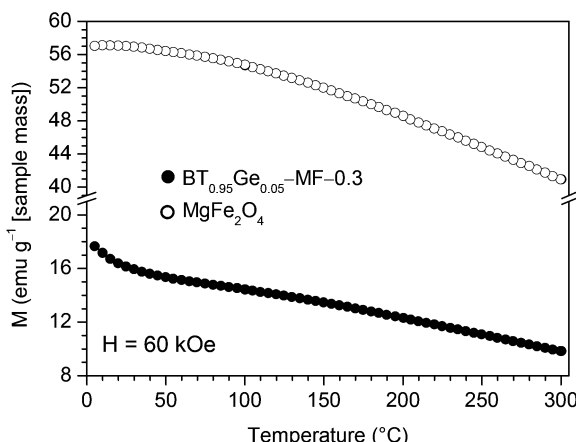


Fig. 10 Temperature dependence (5–300 K) of the magnetization at $H = 60$ kOe under field-cooled (FC) conditions for BT_{0.95}G_{0.05}-MF-0.3 and pure MgFe₂O₄ ceramics both sintered at 1000 °C/1 h.

Room-temperature dielectric measurements between 1 kHz and 13 MHz for BT_{0.95}G_{0.05}-MF-0.3 ceramics sintered under various conditions are shown in Fig. 11. All composite ceramics show slightly decreasing trends in the relative permittivity (ϵ_r) with increasing frequency (Fig. 11A) indicating dielectric dispersion due to the Maxwell-Wagner interface polarisation.^{54,55} The permittivities of conventionally sintered samples increase with rising sintering temperature because of increasing densities and grain-sizes of the ceramics. It is known that the permittivity depends on the porosity and thus on the density of ceramic bodies because of pore-charging effects.^{56,57} The dissipation factor ($\tan \delta$) decreases for samples sintered at ≤ 1100 °C, whereas sintering at 1150 °C and 1200 °C leads to an increase of $\tan \delta$ (Fig. 11B). The two-step sintered ceramic bodies show the lowest dissipation factors and the relative permittivities vary between 238–224 ($T_2 = 1000$ °C) and 201–184 ($T_2 = 900$ °C), respectively. The decrease of the dissipation

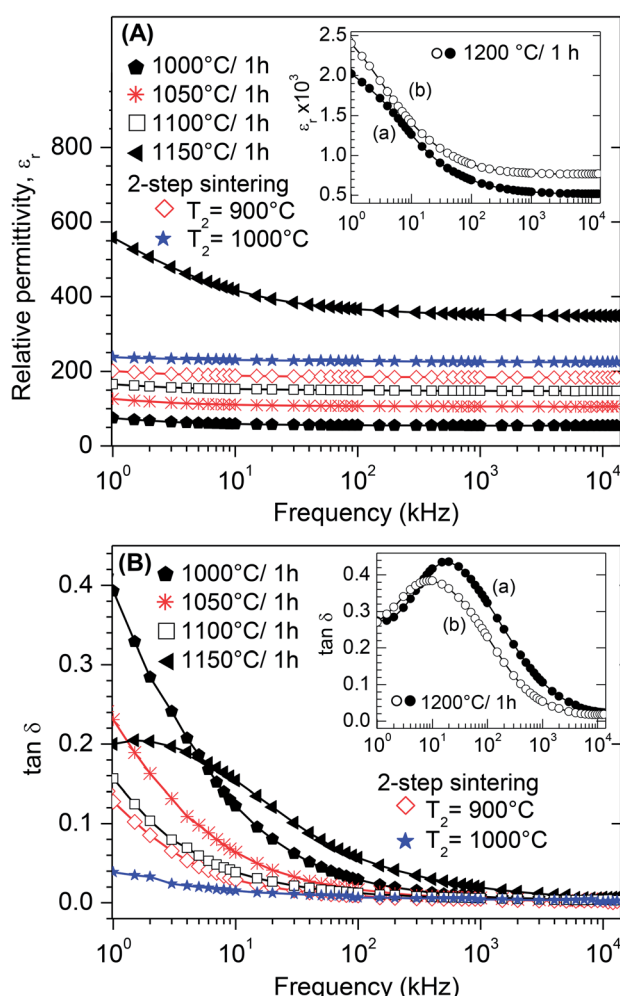


Fig. 11 Frequency dependence of the room-temperature dielectric properties of composite ceramic bodies sintered at the indicated regimes. (A) Real part of the relative permittivity (ϵ_r) of BT_{0.95}G_{0.05}-MF-0.3 ceramics. The inset shows the permittivity of (a) BT_{0.95}G_{0.05}-MF-0.3 and (b) BT_{1.0}G_{0.05}-MF-0.3 ceramics. (B) Dissipation factor ($\tan \delta$) of composite ceramics. The inset shows $\tan \delta$ of (a) BT_{0.95}G_{0.05}-MF-0.3 and (b) BT_{1.0}G_{0.05}-MF-0.3 ceramics.

factor and increase of ε_r of the two-step sintered ceramics, compared to the conventional sintered ones, is most likely due to the improved density and a decrease of lattice defects because of the long soaking time at low temperatures.^{58,59} Dielectric measurements on ceramic bodies of $\text{BT}_{0.95}\text{G}_{0.05}\text{-MF-0.3}$ and $\text{BT}_{1.0}\text{G}_{0.05}\text{-MF-0.3}$ sintered at 1200 °C (see insets in Fig. 11A and B) show that the titanium excess, needed for the suppression of hexagonal BaTiO_3 , only slightly influences the dielectric properties resulting in slightly higher ε_r and lower $\tan \delta$ values.

Fig. 12 demonstrates dielectric measurements of both $\text{BT}_{0.95}\text{G}_{0.05}\text{-MF-0.3}$ and $\text{BT}\text{-MF-0.3}$ (*i.e.* otherwise identical samples with and without BaGeO_3 as sintering additive) composite ceramics after conventional sintering. Considerably higher permittivity values are obtained for $\text{BT}_{0.95}\text{G}_{0.05}\text{-MF-0.3}$ ceramics primarily due to their higher densities caused by the addition of BaGeO_3 .⁶⁰ Up to a sintering temperature of 1150 °C the $\tan \delta$ values of $\text{BT}_{0.95}\text{G}_{0.05}\text{-MF-0.3}$ are significantly lower than for the $\text{BT}\text{-MF-0.3}$ ceramics (inset in Fig. 12). The decrease of $\tan \delta$, resulting from the BaGeO_3 addition, is probably related to the increase in grain boundary resistivity.^{61,62}

The development of the relative permittivity and the dissipation factor between -5 °C and 180 °C at a frequency of 1 kHz for selected $\text{BT}_{0.95}\text{G}_{0.05}\text{-MF-0.3}$ ceramics was additionally studied. Fig. 13A shows ceramics sintered up to 1100 °C, whereas samples sintered at 1150 and 1200 °C are represented in Fig. 13B. The relative permittivities of all samples considerably increase roughly above 50–70 °C and reach a maximum at about 170 °C. Similar temperature dependencies were found in various BaTiO_3 -ferrite ceramics.^{63–69} A clear ferroelectric/paraelectric phase transition of the BaTiO_3 phase was not observed. The ceramic bodies consist of BaTiO_3 grains less than 1.5 μm , which are known to lead to a reduction of the permittivity and to a flattening of the phase transition peak.^{70,71} Furthermore, reactions between BaTiO_3 and MgFe_2O_4 at the grain boundaries lead to impurities and defects resulting in a lower tetragonality. Furthermore, it was shown elsewhere⁷² that

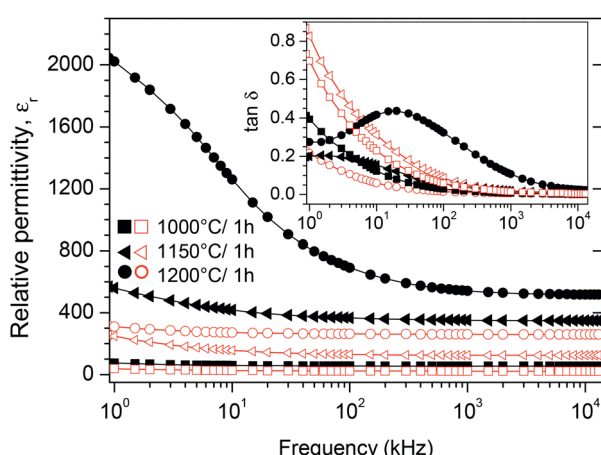


Fig. 12 Frequency dependence of ε_r and $\tan \delta$ at room temperature for $\text{BT}_{0.95}\text{G}_{0.05}\text{-MF-0.3}$ (solid symbols) and $\text{BT}\text{-MF-0.3}$ (open symbols) ceramic bodies conventionally sintered at the indicated temperatures.

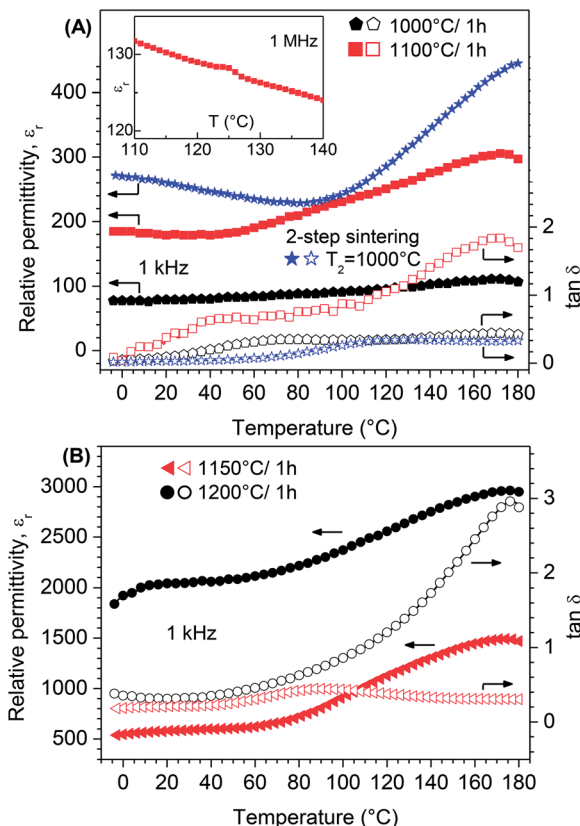


Fig. 13 Temperature dependence of ε_r and $\tan \delta$ at 1 kHz for $\text{BT}_{0.95}\text{G}_{0.05}\text{-MF-0.3}$ ceramic bodies. (A) Conventional sintering at 1000 and 1100 °C for 1 h and two-step-sintering at $T_2 = 1000$ °C/20 h. The inset shows ε_r at 1 MHz after sintering at 1100 °C. (B) Conventional sintering at 1150 and 1200 °C for 1 h.

the ferroelectric/paraelectric phase transition peak continuously decreases and disappears with increasing ferrite content. Investigations by Sakanas *et al.*⁵⁵ and Gupta and Chatterjee⁷³ revealed that the phase transition peaks of BaTiO_3 are more visible at high frequencies because of the space charge polarisation in the composites. In fact our temperature depended dielectric measurements at a higher frequency of 1 MHz showed for a sample sintered at 1100 °C an anomaly between roughly 120 and 130 °C (inset in Fig. 13A) which can be assigned to a ferroelectric/paraelectric phase transition.⁷³

4. Conclusions

The effect of the sintering additive BaGeO_3 on $\text{MgFe}_2\text{O}_4\text{-BaTiO}_3$ composites was investigated. Composite samples with a composition of $0.7 \times (\text{BaTi}_{0.95}\text{Ge}_{0.05}\text{O}_3) - 0.3 \times (\text{MgFe}_2\text{O}_4)$ were prepared by a one-pot Pechini-like synthesis. Calcination at 700 °C leads to a nano-sized powder showing a superparamagnetic behaviour. DTA investigations reveal the formation of a liquid phase with an onset temperature of 1164(3) °C. The addition of BaGeO_3 clearly improved the densification process of compacted powders. Conventional sintering between 1000 and 1200 °C results in ceramic bodies with relative densities of 60–96%. A two-step sintering process at 1000 and



900 °C with a prolonged soaking time of 20 h results in relative bulk densities of 83 and 78% with grains between about 90 and 230 nm. Small traces of $\text{BaFe}_{12}\text{O}_{19}$ appear after sintering at 1150 °C and the partial formation of hexagonal BaTiO_3 is observed at 1200 °C. Magnetic measurements reveal typical ferrimagnetic behaviour with coercivity values up to 70 Oe depending on the sintering procedure. Dielectric measurements show that the addition of BaGeO_3 leads to an increase of the relative permittivity, whereas the dissipation factor slightly decreases. Additionally, it is shown that the sintering regime also influences the dielectric behaviour. Sintering at 1150 °C leads to dense and coarse-grained ceramic bodies possessing high ϵ_r and moderate $\tan \delta$ values over a wide temperature range. On the other hand, fine-grained ceramic bodies with high densities can be obtained after a two-step sintering process showing relative permittivities up to 238 at room-temperature and the lowest $\tan \delta$ values. The resulting composite ceramics are potential candidates for ME applications.

Acknowledgements

Financial support by the German Research Foundation within the Collaborative Research Centre (SFB 762) *Functionality of Oxide Interfaces* is gratefully acknowledged.

Notes and references

- 1 C.-W. Nan, M. I. Bichurin, S. Dong, D. Viehland and G. Srinivasan, *J. Appl. Phys.*, 2008, **103**, 031101.
- 2 J. Ma, J. Hu, Z. Li and C.-W. Nan, *Adv. Mater.*, 2011, **23**, 1062–1087.
- 3 J. F. Scott, *Nat. Mater.*, 2007, **6**, 256–257.
- 4 J. Ryu, S. Priya, K. Uchino and H.-E. Kim, *J. Electroceram.*, 2002, **8**, 107–119.
- 5 R. S. Devan and B. K. Chougule, *J. Appl. Phys.*, 2007, **101**, 014109.
- 6 P. Zhu, Q. Zheng, R. Sun, W. Zhang, J. Gao and C. Wong, *J. Alloys Compd.*, 2014, **614**, 289–296.
- 7 Y. Liu, Y. Wu, D. Li, Y. Zhang, J. Zhang and J. Yang, *J. Mater. Sci.: Mater. Electron.*, 2014, **24**, 1900–1904.
- 8 R. Liu, Y. Thao, R. Huang, Y. Zhao and H. Zhou, *J. Mater. Chem.*, 2010, **20**, 10665–10670.
- 9 L. V. Leonel, J. B. Silva, A. S. Albuquerque, J. D. Ardisson, W. A. A. Macedo and N. D. S. Mohallem, *J. Phys. Chem. Solids*, 2012, **73**, 1362–1371.
- 10 J. van den Boomgaard and R. A. J. Born, *J. Mater. Sci.*, 1978, **13**, 1538–1548.
- 11 M. M. Sutar, A. N. Tarale, S. R. Jigajeni, S. B. Kulkarni, V. R. Reddy and P. B. Joshi, *Solid State Sci.*, 2012, **14**, 1064–1070.
- 12 R. Grigalaitis, M. M. Vijatović Petrović, J. D. Bobić, A. Džunuzović, R. Sobiestianskas, A. Brilingas, B. D. Stojanović and J. Banys, *Ceram. Int.*, 2014, **40**, 6165–6170.
- 13 L. M. Hrib and O. F. Caltun, *J. Alloys Compd.*, 2011, **509**, 6644–6648.
- 14 S. Y. Tan, S. R. Shannigrahi, S. H. Tan and F. E. H. Tay, *J. Appl. Phys.*, 2008, **103**, 094105.
- 15 R. Tadi, Y.-I. Kim and K.-S. Ryu, *J. Korean Phys. Soc.*, 2012, **61**, 1545–1549.
- 16 R. Tadi, Y.-I. Kim, D. Sarkar, C. Kim and K.-S. Ryu, *J. Magn. Magn. Mater.*, 2011, **323**, 564–568.
- 17 R. Köferstein, T. Walther, D. Hesse and S. G. Ebbinghaus, *J. Alloys Compd.*, 2015, **638**, 141–147.
- 18 J.-H. Lee, Y.-W. Heo, J.-A. Lee, Y.-D. Ryoo, J.-J. Kim and S.-H. Cho, *Solid State Ionics*, 1997, **101–103**, 787–791.
- 19 D. Völtzke and H.-P. Abicht, *Solid State Sci.*, 2000, **2**, 149–159.
- 20 R. Köferstein, L. Jäger and S. G. Ebbinghaus, *J. Mater. Sci.*, 2010, **45**, 6521–6527.
- 21 L. Geske, V. Lorenz, T. Müller, L. Jäger, H. Beige, H.-P. Abicht and V. Mueller, *J. Eur. Ceram. Soc.*, 2005, **25**, 2537–2542.
- 22 W. Ling, H. Zhang, Y. Li, D. Chen, Q. Wen and J. Shen, *J. Appl. Phys.*, 2010, **107**, 09D911.
- 23 A. Francis and W. Daoush, *J. Mater. Process. Technol.*, 2007, **181**, 213–216.
- 24 N. Kitahara, H. Kageyama, T. Kawasaki, K. Abe, H. Itoh and J. Takahashi, *J. Ceram. Soc. Jpn.*, 2013, **121**, 54–61.
- 25 K. Li, D.-L. Shi, Y. Zhu, Y. Wang, H. L. Chan and S. Peng, *Mater. Chem. Phys.*, 2013, **143**, 34–40.
- 26 R. Köferstein, L. Jäger, M. Zenkner, F. J. Garcia-Garcia and S. G. Ebbinghaus, *J. Mater. Sci.*, 2010, **45**, 3784–3790.
- 27 Y.-C. Lee, W.-H. Lu, S.-H. Wang and C.-W. Lin, *Int. J. Miner., Metall. Mater.*, 2009, **16**, 124–127.
- 28 *Program WinXPOW v2.11*, Stoe & Cie GmbH, Darmstadt, 2004.
- 29 K. Kamishima, Y. Nagashima, K. Kakizaki, N. Hiratsuka, K. Watanabe, T. Mise, H. Naganuma and S. Okamura, *J. Phys. Soc. Jpn.*, 2008, **77**, 064801.
- 30 R. Köferstein, L. Jäger, M. Zenkner and H.-P. Abicht, *J. Mater. Sci.*, 2008, **43**, 832–838.
- 31 M. Zenkner, L. Jäger, R. Köferstein and H.-P. Abicht, *Solid State Sci.*, 2008, **10**, 1556–1562.
- 32 J. P. Guha and D. Kolar, *J. Mater. Sci.*, 1972, **7**, 1192–1196.
- 33 International Centre for Diffraction Data, PDF-2/Release 2008, BaTiO_3 [00-81-2201]_{tetragonal}, BaTiO_3 [00-82-1175]_{hexagonal}, MgFe_2O_4 [00-71-1232]_{cubic}, $\text{BaFe}_{12}\text{O}_{19}$ [00-84-757]_{hexagonal}, BaCO_3 [00-5-378]_{orthorhombic}, BaGeO_3 [01-075-4952]_{monoclinic}.
- 34 V. D. Allred, S. R. Buxton and J. P. McBride, *J. Phys. Chem.*, 1957, **61**, 117–120.
- 35 W. Schatt, *Sintervorgänge*, VDI-Verlag, Düsseldorf, 1992, pp. 78–100.
- 36 W. Schatt, *Z. Metalkde.*, 1989, **80**, 809–816.
- 37 W. Schatt and E. Friedrich, *Key Eng. Mater.*, 1988, **29–31**, 73–88.
- 38 D. Völtzke and H.-P. Abicht, *Solid State Sci.*, 2000, **2**, 149–159.
- 39 R. Köferstein, L. Jäger, M. Zenkner, T. Müller and H.-P. Abicht, *Mater. Chem. Phys.*, 2008, **112**, 531–535.
- 40 A. Recnik and D. Kolar, *J. Am. Ceram. Soc.*, 1996, **79**, 1015–1018.
- 41 I.-W. Chen and X.-H. Wang, *Nature*, 2000, **404**, 168–171.
- 42 S. Lee, C. A. Randall and Z.-K. Liu, *J. Am. Ceram. Soc.*, 2007, **90**, 2589–2594.



43 T. A. Vanderah, J. M. Loezos and R. S. Roth, *J. Solid State Chem.*, 1996, **121**, 38–50.

44 R. Böttcher, H. T. Langhammer, T. Müller and H.-P. Abicht, *J. Phys.: Condens. Matter*, 2008, **20**, 505209.

45 N. Maso, H. Beltran, E. Cordoncillo, P. Escribano and A. R. West, *J. Mater. Chem.*, 2006, **16**, 1626–1633.

46 S. Jayanthi and T. R. N. Kutty, *J. Mater. Sci.: Mater. Electron.*, 2008, **19**, 615–626.

47 J. Jeong and Y. H. Han, *Phys. Chem. Chem. Phys.*, 2003, **5**, 2264–2267.

48 V. A. M. Brabers, A. A. E. Stevens, J. H. J. Dalderop and Z. Simsa, *J. Magn. Magn. Mater.*, 1999, **196–197**, 312–314.

49 M. H. Shams, S. M. A. Salehi and A. Ghasemi, *Mater. Lett.*, 2008, **62**, 1732–1733.

50 R. Köferstein, T. Walther, D. Hesse and S. G. Ebbinghaus, *J. Mater. Sci.*, 2013, **48**, 6509–6518.

51 S. Ray, P. Mahadevan, S. Mandal, S. R. Krishnakumar, C. S. Kuroda, T. Sasaki, T. Taniyama and M. Itoh, *Phys. Rev. B: Condens. Matter Mater. Phys.*, 2008, **77**, 104416.

52 X. K. Wei, Y. T. Su, Y. Sui, Q. H. Zhang, Y. Yao, C. Q. Jin and R. C. Yu, *J. Appl. Phys.*, 2011, **110**, 114112.

53 S. Qiu, W. Li, Y. Liu, G. Liu, Y. Wu and N. Chen, *Trans. Nonferrous Met. Soc. China*, 2010, **20**, 1911–1915.

54 K. W. Wagner, *Arch. Elektrotech.*, 2014, **2**, 371–387.

55 A. Sakanas, R. Grigalaitis, J. Banys, L. Mitoseriu, V. Buscaglia and P. Nanni, *J. Alloys Compd.*, 2014, **602**, 241–247.

56 K. Okazaki and K. Nagata, *J. Am. Ceram. Soc.*, 1973, **56**, 82–86.

57 C.-C. Hsueh, M. L. Mecartney, W. B. Harrison, M. R. B. Hanson and B. G. Koepke, *J. Mater. Sci. Lett.*, 1989, **8**, 1209–1216.

58 J. S. Kim, S. Y. Lee, H. J. Lee, C. W. Ahn, I. W. Kim and M. S. Jang, *J. Electroceram.*, 2008, **21**, 633–636.

59 Y. Noguchi, I. Miwa, Y. Goshima and M. Miyayama, *Jpn. J. Appl. Phys.*, 2000, **39**, L1259–L1262.

60 R. W. Rice, *Porosity of ceramics*, M. Dekker Inc., New York, 1998, pp. 354–359.

61 P. Kantha, N. Pisitpipathsin, K. Pengpat, G. Rujjanagul, R. Guo and A. S. Bhalla, *Ferroelectrics*, 2011, **425**, 27–38.

62 F. Amaral, L. C. Costa and M. A. Valente, *J. Non-Cryst. Solids*, 2011, **357**, 775–781.

63 V. V. Shartsman, F. Alawneh, P. Borisov, D. Kozodaev and D. C. Lupascu, *Smart Mater. Struct.*, 2011, **20**, 075006.

64 L. Curecheriu, P. Postolache, V. Buscaglia, N. Hochidan, M. Alexe and L. Mitoseriu, *Phase Transform.*, 2013, **86**, 670–680.

65 C. M. Kanamadi, J. S. Kim, H. K. Yang, B. K. Moon, B. C. Choi and J. H. Jeong, *Appl. Phys. A*, 2009, **97**, 575–580.

66 X. Qi, J. Zhou, Z. Yue, Z. Gui, L. Li and S. Buddhudu, *Adv. Funct. Mater.*, 2004, **14**, 920–926.

67 L. P. Curecheriu, M. T. Buscaglia, V. Buscaglia, L. Mitoseriu, P. Postolache, A. Ianculescu and P. Nanni, *J. Appl. Phys.*, 2010, **107**, 104106.

68 K. Raidongia, A. Nag, A. Sundaresan and C. N. R. Rao, *Appl. Phys. Lett.*, 2010, **97**, 062904.

69 D. Hgosh, H. Han, J. C. Nino, G. Subhash and J. L. Jones, *J. Am. Ceram. Soc.*, 2012, **95**, 2504–2509.

70 G. Arlt, D. Hennings and G. de With, *J. Appl. Phys.*, 1985, **58**, 1619–1625.

71 R. Köferstein, L. Jäger, M. Zenkner and S. G. Ebbinghaus, *Mater. Chem. Phys.*, 2010, **119**, 118–122.

72 Z. Yu and C. Ang, *J. Mater. Sci.: Mater. Electron.*, 2002, **13**, 193–196.

73 A. Gupta and R. Chatterjee, *J. Eur. Ceram. Soc.*, 2013, **33**, 1017–1022.

